Supporting Information for "Sub-microsecond spectroscopy of lightning-like discharges: exploring new time regimes"

N. Kieu[1], F. J. Gordillo-Vázquez[1], M. Passas[1], J. Sánchez[1], F. J. Pérez-Invernón[2], A. Luque[1], J. Montanyá[3], and H. Christian[4]

[1]Instituto de Astrofísica de Andalucía (IAA), CSIC, PO Box 3004, 18080 Granada, Spain

[2]Institut für Physik der Atmosphäre, Deutsches Zentrum für Luft- und Raumfahrt, Wessling, Germany

[3]Department of Electrical Engineering, Universitat Politécnica de Catalunya, C. Colom, 1, Terrassa, Spain

[4]Earth System Science Center, University of Alabama Huntsville, Huntsville, AL, USA

Contents of this file

1. Text S1

2. Figures S1 to S20

Introduction We include here the shape of the typical voltages and currents used to generate the different lightning-like discharges investigated in this study (Figure S1 through S3). We also provide the equilibrium composition in meter long (Switching (SI) and Lightning (LI) Impulse modes of a Marx generator) and small (centimeter long) air thermal plasmas at 1 atm for the times for which electron density and temperature are measured (Figure S4 through S7). We present calculated synthetic spectra of lightning-like discharges assuming equilibrium composition at 1 atm (Figures S8 through 10) and compare synthetic with measured spectra of the SI, LI and small spark discharges (Figures S11 through S13). Figures S14 through S16 show the δ_p factor (described in the main paper), the total pressure and the partial pressures due to electrons, ions and neutrals together with an estimation of the shock front position and velocity as a function of time for meter long discharges (SI and LI) and for a small (4 cm long) spark discharge. Figure S17 shows the self-absorption (SA) coefficient ($0 \leq \mathrm{SA} \leq 1$) of the 647 nm and 661 nm singly ionized N II lines as a function of time. Figures S18 and S19 show the typical shape of the H_α line and of the 647 nm and 661 nm ion lines to illustrate the procedures followed to derive the electron density and temperature. Finally, Figure S20 shows a raw image spectrum of the LI mode of the Marx generator. Some details of the equilibrium, black body continuum (background) dynamics, synthetic spectra calculations and the procedure followed to derive a line spectrum from a raw image spectrum are presented in Text S1.

Text S1. The measured voltages and currents used to generate the different lightning-like discharges investigated in this study are shown in Figure S1, Figure S2 and Figure S3. The camera buffer allowed us to capture images of the discharge before the trigger takes place, although this was not always possible.

Local thermal equilibrium (LTE) composition of atmospheric pressure lightning-like air plasmas (78 % N_2 and 22 % O_2) is calculated and shown here in order to interpret the different features found in the measured time resolved spectra of this work and to quantify possible departures of the measured electron densities from equilibrium. The equilibrium calculations are performed in the temperature range 1000 - 35000 K with a method based upon the mass action law and the chemical base concept (Godin & Trépanier, 2004; Teulet et al., 2009). We have assumed a relative humidity (RH) of 50 % that corresponds to the ambient RH measured in the laboratory during experiments. The chemical species considered were 14 atomic, 24 diatomic and 44 polyatomic species including electrons, negative ions and single and double positive ions. Internal partition functions were also calculated for atoms, diatomic and polyatomic molecules as well as for positive and negative ions.

Comparisons between measured electron densities and equilibrium concentration of electrons are shown in Figure S4 (SI meter long discharge), Figure S5 (LI meter long discharge) and Figure S6 (small - 4 cm - spark). Figure S4 - Figure S6 also present equilibrium concentrations at 1 atm of key neutral and ionic species in the humid air plasma channel formed by different lightning-like discharges in the range of measured temperatures ($\simeq$ 17000 K - $\simeq$ 30000 K). Figure S7 shows calculated equilibrium concentration for a selected

number of species in the entire range of temperatures considered in the calculations (1000 K - 35000 K). The concentration of species like nitrogen oxide (NO) reaches its maximum at $\simeq$ 3300 K, that is, well below the minimum measured temperature.

Synthetic spectra of atmospheric pressure LTE plasmas of humid air at 1 atm are shown in Figure S8 (35000 K - 30000 K), Figure S9 (29000 K - 18000 K) and Figure S10 (16000 K - 8000 K). We have calculated synthetic spectra considering the more abundant neutral atomic (H I, N I, O I) and molecular (N_2) species and atomic ion species (N II, NIII, O II, O III). We have assumed Boltzmann equilibrium for the electronically excited atomic and molecular states and for the vibrational levels of the molecular N_2 included in the spectra. Synthetic spectra include all the tabulated observed optical transitions of the considered neutral atoms and atomic ions (Kramida et al., 2019). For N_2, the synthetic spectra include the first positive system (FPS) in the visible - near-infrared (500 - 1500 nm), second positive system (SPS) in the near-ultraviolet - blue (250 - 450 nm) and the Lyman Birge Hopfield system in the vacuum ultraviolet (120 - 230 nm). The emission intensity of a spectral line from an upper energy level i to a lower energy level j can be written as $I_{ij} = (1/4\pi)\ h\ \nu_{ij}\ A_{ij}\ N_i$, where h is the Planck's constant and ν_{ij} is the frequency of the emitted photon. The number density of atoms / ions in the upper energy level i, N_i, is $N_i = (Ng_ik/Z(T))exp(\epsilon_i/k_BT)$, where k_B is the Boltzmann constant, N is the total number density of atoms / ions of each considered species (N I, O I, H I, ...) and $Z(T)$ is the corresponding partition function (Godin & Trépanier, 2004; Teulet et al., 2009).

Lines dominated by Instrument and / or Doppler broadening exhibit a Gaussian profile. However, when Stark broadening dominates (for sufficiently high electron densities $\geq 10^{16}$ cm^{-3}), the spectral line profile exhibits a Lorentzian shape. The calculated synthetic spectra shown in this supplementary material include convolved Instrumental ($\Delta\lambda_I$), Doppler ($\Delta\lambda_D$) and Stark ($\Delta\lambda_S$) full width broadenings of spectral (hydrogenic and nonhydrogenic) lines associated with neutrals and singly ionized ions. Synthetic spectra assume that spectral lines have a Lorentzian shape with a full width at half maximum given by $\Delta\lambda_{Synthetic} = 0.5 \times \Delta\lambda_S + \sqrt{(0.5\Delta\lambda_S)^2 + \Delta\lambda_I^2}$ since in our conditions we have that $\Delta\lambda_S \gg \Delta\lambda_I$ and $\Delta\lambda_I \gg \Delta\lambda_D$ (Nikiforov et al., 2015).

The nonhydrogenic Stark broadening is predominantly caused by electrons so that we use equation (13.14) in Bekefi (1976) where the electron impact approximation is assumed and corrected for the relatively unimportant quasistatic ion broadening (Bekefi, 1976). A comprehensive list of coefficients needed to compute nonhydrogenic Stark broadening from expression (13.14) in Bekefi (1976) is given in Table 4-5 of Griem (1964).

The limited accuracy of our synthetic spectra is mainly due to inaccurate data and / or to the complete lack of data needed to calculate spectra. For instance, Stark broading coefficients for the neutral lines 648.17 nm, 648.27 nm, 648.37 nm and 648.48 nm are not available in Table 4-5 of Griem (1964) and we selected instead the available coefficients of the closest neutral N I line in 537.20 nm. In addition, the Einstein coefficients (A) of the N I lines 648.17 nm, 648.27 nm, 648.37 nm and 648.48 nm are not very accurate (category "C" in Kramida et al. (2019)). We applied a reduction of 77 % to the Einstein coefficient of the neutral N I line at 648.27 nm and did not consider the other three (less

intense) lines. This is justified so that the synthetic and measured spectra of the small spark match at 2.890 μs when a pressure of $\simeq$ 1 atm is reached in the spark channel (see Figure 3(c) of the main paper and lower right panel of Figure S13). However, for the investigated meter long discharges (SI and LI) we find that room pressure is not yet reached for the last accessible times (see Figure 3(a) and 3(b) of the main paper) and, consequently, their spectra can not be used to estimate the reduction of the A coefficient of the neutral N I line at 648.27 nm.

Stark broadening of hydrogenic lines like H_α is implemented by using $N_e = C(N_e, T)\Delta\lambda_S^{3/2}$ (Griem, 1964) where $\Delta\lambda_S^{3/2}$ is the full Stark width and $C(N_e, T)$ is a coefficient that is only a weak function of the electron density. This expression combines, in a approximate form, the broadening due to electrons and that due to the ion dynamics. Values of $C(N_e, T)$ for several hydrogen lines (including H_α) are summarized in Table 14-1 of Griem (1964).

Stark broadening of molecular species is not considered since molecules will only be present at low temperatures when the ionization degree and electron density are such that Stark broadening is no longer the dominant broadening mechanism. For the case of double ionized N III ions, no Stark broadening coefficients are available. We have considered an arbitrary Stark broadening of 0.1 nm convolved with the instrumenal broadening.

The calculated synthetic spectra also include the contribution from possible black body (continuum) emission, which has been considered as a fitting parameter of the synthetic to the measured spectra.

Synthetic spectra in Figure S8 exhibit two strong singly ionized N II lines at 648.20 nm and 661.05 nm and a weak H_α line (656.27 nm) that slightly grows with decreasing temperature from 35000 K to 30000 K. We see that the spectrum for 35000 K shows two small wrinkles at 645.41 nm and 646.70 nm (corresponding to two doubly ionized N III spectral lines). Also for 35000 K, the two weak features at 656.52 nm and 657.11 nm are due to two singly ionized O II spectral lines. These O II emissions slightly affect the shape of the line at 656.2 (H_α) at high temperatures. Black body emission is especially noticeable in these high temperature spectra.

In Figure S9 we see that the spectrum for 18000 K shows two weak humps at 645.44 nm and 645.59 nm corresponding to two neutral O I spectral lines. These O I features become less noticeable at 29000 K due to increasing ionization. Finally, the weak features shown at 649.12 nm and 649.95 nm for 18000 K are associated to two neutral N I lines that fade away with increasing temperatures. Black body emission in this temperature range (18000 - 29000 K) is much less important than for higher temperatures (see Figure S8).

Figure S10 shows synthetic spectra calculated for the lowest considered temperature range (8000 - 16000 K). The line at 660.8 nm corresponds to molecular emission. In particular, it corresponds to a vibrational transition ($v^{'} = 6 \rightarrow v^{''} = 3$) of the first positive system (FPS) of molecular nitrogen (N_2) that remains visible at 8000 K. The H_α line (656.27 nm) starts to be apparent from $\simeq$ 8000 K (very narrow) and it keeps growing up to $\simeq$ 20000 K (see Figure S9) when it begins to decline. Around $\simeq$ 18000 K - 20000 (see Figure S9) the 648.20 nm N II ion line is replaced by a N I multiplet (648.17, 648.27,

648.37 and 648.48 nm) that remains active for about 10 μs for the SI discharge and during tens of μs in the case of the LI discharge.

Finally, Figure S11-Figure S13 present a comparison of synthetic spectra with measured ones for meter long discharges (SI in Figure S11 and LI in Figure S12) and for the small spark (Figure S13). Synthetic and measured spectra do not completely agree. We think that this is mainly due to two reasons: (a) unavailability and / or lack of accurate basic data (Einstein coefficients and Stark broadening parameters) needed to compute reliable synthetic spectra based on equilibrium concentrations of excited species and (b) to the fact that the ultra-high speed recorded spectra include light emissions from the hot and over-pressure shock front and from the hot core air plasma channel (kept at a lower gas density than ambient) behind the shock front.

Regarding point (b) (over-pressure hot shock front and hot channel core), it is interesting to analyze Figure S11 (for the SI meter long discharge) and Figure S13 (for the small spark). Both of them display spectra corresponding to the six times shown in, respectively, Figure 1(b) and Figure 1(f) of the main paper. Figure S11 shows that synthetic and measured spectra nicely agree at -0.120 μs (the earliest time before triggering that we could evaluate), a time for which we could measure the temperature but not the corresponding electron density. The match of spectra at -0.120 μs suggests that the discharge channel over-pressure (with respect to the ambient 1 atm pressure) is still very small and that the electron density in the plasma channel would be very close to the equilibrium electron density at 1 atm (used to compute the synthetic spectra). However, 0.476 μs afterwards (or 0.356 μs after triggering) the channel over-pressure (and black body radiation) be-

comes very important (see Figure S11 for 32000 K) with $\delta_p > 4$ (see Figure 3(b) of the main paper and Figure S14 in this supplementary material), which is reflected in the low H_α signal of the synthetic spectra. The over-pressure in the discharge channel diminishes as time progresses but it still remains ($\delta_p \simeq 2$) at 2.260 μs (see Figure S14 in this supplementary material). Thus, time-resolved spectroscopy indicates that continuum radiation is negligible at very early (pre-trigger) times, reaches a maximum at about 0.356 μs after triggering and tend to decrease with increasing times (lower measured temperature).

In the case of Figure S12 for the LI lightning-like discharge, we see that black body continuum emission at trigger time (0.0 μs) - associated to 31000 K - is considerably smaller than at lower temperatures.

The sequence of six synthetic and measured spectra displayed in Figure S13 for the case of a small spark indicates that the over-pressure ($\delta_p > 3$, see Figure 3(c) of the main paper and Figure S16 in this supplementary material) was already set in the first time (0.510 μs at 33000 K) we could evaluate. In the case of the small spark, the over-pressure in the channel rapidly evolves towards ambient pressure in less than 3 μs as we can see in the spectra shown in Figure S13 for 2.890 μs for which $\delta_p \simeq 1$ (see Fig. 3(c) of the main paper and Figure S16 in this supplementary material). The dynamics of the black body continuum (or background) shown in Figure S13 is similar to that of Figure S11 and S12, except for the fact that black body radiation is already noticeable in the first time (0.510 μs) of the small spark spectra but, as in Figure S11 and S12, it tends to dissapear as time progresses and the pressure in the plasma channel returns to ambient values.

Figures S14 through S16 show the time evolution of the total and partial pressures (due to electrons, ions and neutrals) in the discharge channel shock front for, respectively, the meter long discharges SI (Figure S14) and LI (Figure S15), and for the small spark discharge (Figure S16). Once the over-pressure factor δ_p is experimentally determined, we can approximately compute the total and partial pressures by using the ideal gas law with the concentrations of electrons, ions and neutrals multiplied by δ_p. Figures S14 - S16 also include the approximate position (R) and speed (U) of the hydrodynamic shock front estimated with $R = \alpha\ t^{0.5}$ and $U = 0.5 \times \alpha\ \mathrm{t}^{-0.5}$ resulting from the solution of the Rankine-Hugoniot equations to evaluate the discrate changes in the mass density, pressure and velocity across the shock front produced after electrical breakdown (Zahn et al., 1982). The values of the parameter α is estimated from $\alpha = (2\mathrm{E}/(\pi\rho\ 0.63))^{0.25}$ where E is the total injected electric energy per unit length (in J m^{-1}) (see the main paper and the captions of Figures S1, S2 and S3) and ρ is the ambient air density in the laboratory experiments (Zahn et al., 1982). In our case, α (small spark) = 2.29 m $\mathrm{s}^{-0.5}$, α (meter long SI discharge) = 2.89 m $\mathrm{s}^{-0.5}$ and α (meter long LI discharge) = 4.93 m $\mathrm{s}^{-0.5}$. The adopted values for ρ were 1.10 kg m^{-3} for the small spark experiments at the IAA-CSIC in Granada (94000 Pa, 50 % and 293 K) and 1.17 kg m^{-3} for meter long discharge experiments in Barcelona (101000 Pa, 50 %, 293 K). The values of U and R decrease and increase monotonically as time progresses with U reaching values of about 10 times the speed of sound in air (see Figures S15 for the LI discharge). The shock front position R should approximately indicate the location where over-pressure is measured.

Figure S17 shows the self-absorption (SA) coefficient of the 647 nm and 661 nm singly ionized N II lines as a function of time for meter long discharges SI (top panel) and LI (middle panel), and for a small (4 cm long) spark discharge (bottom panel). We have evaluated the SA under the assumption of a homogenous plasma (El Sherbini et al., 2005). The SA is defined as the ratio of the measured peak intensity to the value of the line intensity in absence of self-absorption. SA is equal to one if the the line is optically thin, while it decreases to zero as the line becomes optically thick. Thus, the SA(s) are obtained from $\Delta\lambda$ / $\Delta\lambda_0 = (\mathrm{SA})^{\beta}$ with β = -0.54 (El Sherbini et al., 2005) and $\Delta\lambda$ and $\Delta\lambda_0$ being the full width at half maximum (FWHM) of the observed (measured) ion line(s) and the calculated FWHM of the true ion line (without self-absorption), respectively. Note that the calculated FWHM of the true ion lines use the measured electron density obtained from the H_α line, which is known to be insignificantly affected by self-absorption unless the amount of hydrogen is very high, which is not the case in air (El Sherbini et al., 2005; Parigger et al., 2014). We have considered that $\Delta\lambda_0$ results from the convolution of calculated instrumental and Stark effect FWHM(s) of the two N II ionic lines which self-absorption coefficients are searched for. The calculation procedure of Stark FWHMs was previously commented. According to Figure S17, the values of the SA coefficient grow towards one with increasing time (or decreasing pressure in the discharge channel). This is especially evident for the LI discharge (middle panel of Figure S17) where the the SA increases from 0.2 to $\geq$ 0.8 as the pressure in the channel decreases (see Figures S15).

Finally, Figures S18 and S19 illustrate the method followed to derive the electron density and electron temperature. For the electron density, the black body background inherited

from the spark core radiation is first subtracted in Figure S18 to not overestimate the electron density. As we are considering a small bandwidth (645 − 664 nm) of the spark spectrum, we have reasonably assumed that the black body contribution is flat in the narrow spectral bandwidth investigated and it is different at every time stage of the spark. As the spectrum is sometimes noisy, we estimated the blackbody radiation background as the mean value of the first 5 lowest values (starting in 645 nm) of the line spectra at any instant of time. So, for every time stage of the spark, we subtracted this blackbody radiation background from its discharge line spectrum before estimating the electron density.

Due to the large electron density the broadening of the H_α line is large and it should be considered that it extends over the entire ($\simeq$ 20 nm) spectral range covered in our ultra high speed observations at 2.1 Mfps. Once the shape of the H_α (green dotted line) is determined, we compute the full width at half area (FWHA) (see grey shadow) under the green dotted line used to derived the measured electron density. The FWHA for the H_α is much less influenced by ion dynamics than the full width at half maximum (FWHM) and, consequently, it is a more reliable procedure (than using the FWHM) to obtain the electron density from the H_α line.

Figure S19 shows that to evaluate the electron temperature we only consider the intensity signal above the black body background (see red dots) and we consider the total area (not the peak maximum) under the intensities of the 647 nm and 661 nm singly ionized N II lines.

Figure S20 shows a raw image (8 pixels height and 1024 pixels wide) spectrum of the LI mode discharge. The method we used to derive line spectra from raw spectra is the same as the one we described before (Passas et al., 2019): (1) distortion correction, to straighten the curved raw spectrum; (2) wavelength calibration, to assign an absolute wavelength to each pixel of the CMOS sensor; (3) flux calibration, to provide the spectral sensitivity of the spectrograph; and (4) data reduction.

In this case (using a different difraction grating to that used in Passas et al. (2019)), for steps (1) and (2), we recorded the spectrum of two commercial neon and argon spectral lamps. Then, we trimmed these images so all spectral lines appeared in every row of the spectrum. We identified the corresponding wavelengths by comparing the distances between the spectral lines to the gaps that neon and argon spectra show according to NIST atomic spectra databases. Finally, to straighten the spectrum, we assigned the central pixel of each spectral line to a single wavelength for every row of the spectral image with a Python code we have implemented, that generates a calibration matrix that will be used hereinafter to correct the distorted spectra recorded with GALIUS, associating every pixel coordinate of the CMOS to an absolute wavelength. This calibration matrix is calculated every time we perform a new set of measurements. For step (3) we recorded the spectral radiance of a halogen tungsten spectral lamp (QTH) at 50 fps located at 60 cm from the collector lens of GALIUS using the difraction grating using here, and corrected its distortion according to steps (1) and (2), so we have the straightened QTH response. Then we repeated these measurements with a calibrated Jobin Yvon HORIBA FHR1000 spectrometer using the same calibration setup. From these calculations, we obtained

the difraction grating instrument function that allows us to do a relative flux correction of the raw signal. Finally, for step (4) we subtracted the black image background (an image without any spectrum) from the raw image. Then, we applied the wavelength calibration matrix calculated in steps (1) and (2), to straighten the spectrum and assign a wavelength to every column of the CMOS image. Then, we divided this image by the instrument function calculated in (3) so we corrected the CMOS inhomogeneities and the different response of the pixels to different wavelengths. Last step was to sum up the 8 rows of the reduced spectrum so we got the line spectra shown in the main manuscript.

References

Bekefi, G. (Ed.). (1976). *Principles of laser plasmas*. John Wiley and Sons.

El Sherbini, A., El Sherbini, T. M., Hegazy, H., Cristoforetti, G., Legnaioli, S., Palleschi, V., et al. (2005). Evaluation of self-absorption coefficients of aluminum emission lines in laser-induced breakdown spectroscopy measurements. *Spectrochimica Acta Part B: Atomic Spectroscopy*, *60*(12), 1573–1579.

Godin, D., & Trépanier, J. (2004). A robust and efficient method for the computation of equilibrium composition in gaseous mixtures. *Plasma chemistry and plasma processing*, *24*(3), 447–473.

Griem, H. (1964). *Plasma spectroscopy*. McGraw-Hill.

Kramida, A., Yu. Ralchenko, Reader, J., & and NIST ASD Team. (2019). *Nist atomic spectra database (ver. 5.7.1)*. NIST Atomic Spectra Database (ver. 5.7.1), [Online]. Available: `https://physics.nist.gov/asd` [2020, January 22]. National Institute of Standards and Technology, Gaithersburg, MD.

Nikiforov, A. Y., Leys, C., Gonzalez, M., & Walsh, J. (2015). Electron density measurement in atmospheric pressure plasma jets: Stark broadening of hydrogenated and non-hydrogenated lines. *Plasma Sources Science and Technology*, *24*(3), 034001.

Parigger, C., Swafford, L., Surmick, D., Witte, M., Woods, A., & Gautam, G. (2014). Hydrogen alpha self-absorption effects in laser-induced air plasma. In *Journal of physics: Conference series* (Vol. 548, p. 012043).

Passas, M., Sánchez, J., Kieu, T. N., Sánchez-Blanco, E., & Gordillo-Vázquez, F. J. (2019). Galius: an ultrafast imaging spectrograph for the study of lightning. *Applied optics*, *58*(29), 8002–8006.

Teulet, P., Gonzalez, J. J., Mercado-Cabrera, A., Cressault, Y., & Gleizes, A. (2009). One-dimensional hydro-kinetic modelling of the decaying arc in air-PA66-copper mixtures: I. Chemical kinetics, thermodynamics, transport and radiative properties. *J. Phys. D*, *42*(17), 175201.

Zahn, M., Forster, E. O., Kelley, E. F., & Hebner Jr, R. E. (1982). Hydrodynamic shock wave propagation after electrical breakdown. *Journal of Electrostatics*, *12*, 535–546.

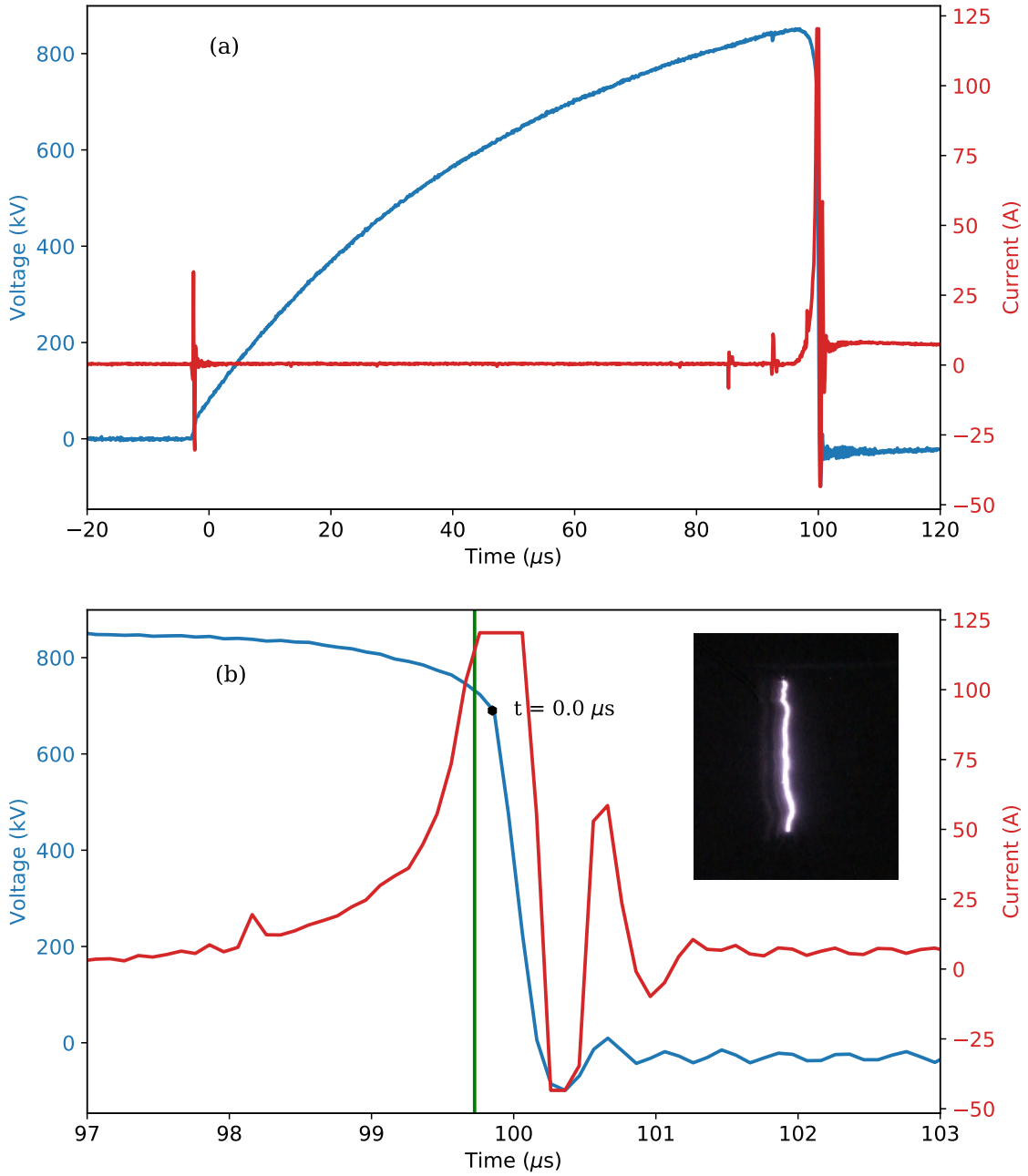

Figure S1. Measured voltage (blue line) and current (red line) during the generation of the Switching Impulse (SI) mode discharge of the Marx generator. (a) Complete time evolution of the voltage and current. (b) Zoom in for a close view of the rise / decay region around 100 μs with an image showing the typical appearance of the SI discharge. The green line in (b) indicates the time of the first recorded spectrum. The black dot in (b) indicates the triggering time. The injected electric energy is 81 J or 81 J/m (since the discharge length is $\simeq$ 1 m).

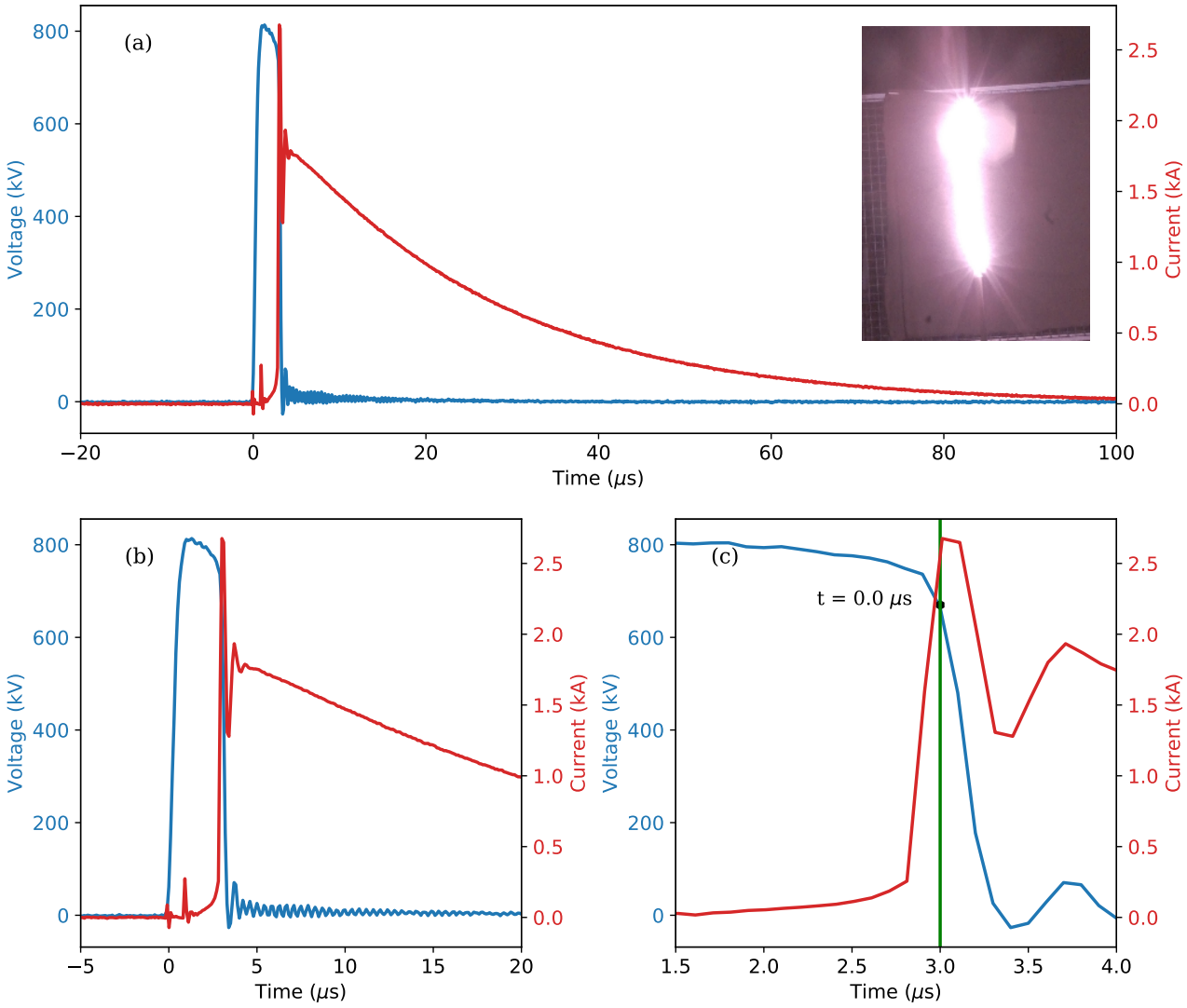

Figure S2. Measured voltage (blue line) and current (red line) during the generation of the Lightning Impulse (LI) mode discharge of the Marx generator. Panels (a), (b) and (c) show time intervals between, respectively, -20 μs and 100 μs, -5 μs and 20 μs, and 1.5 μs and 5 μs. The inset image in (a) shows the typical appearance of the LI discharge. The green line in (c) indicates the time of the first recorded spectrum. The black dot in (c) indicates the triggering time. The injected electric energy is 684 J or 684 J/m (since the discharge length is $\simeq$ 1 m).

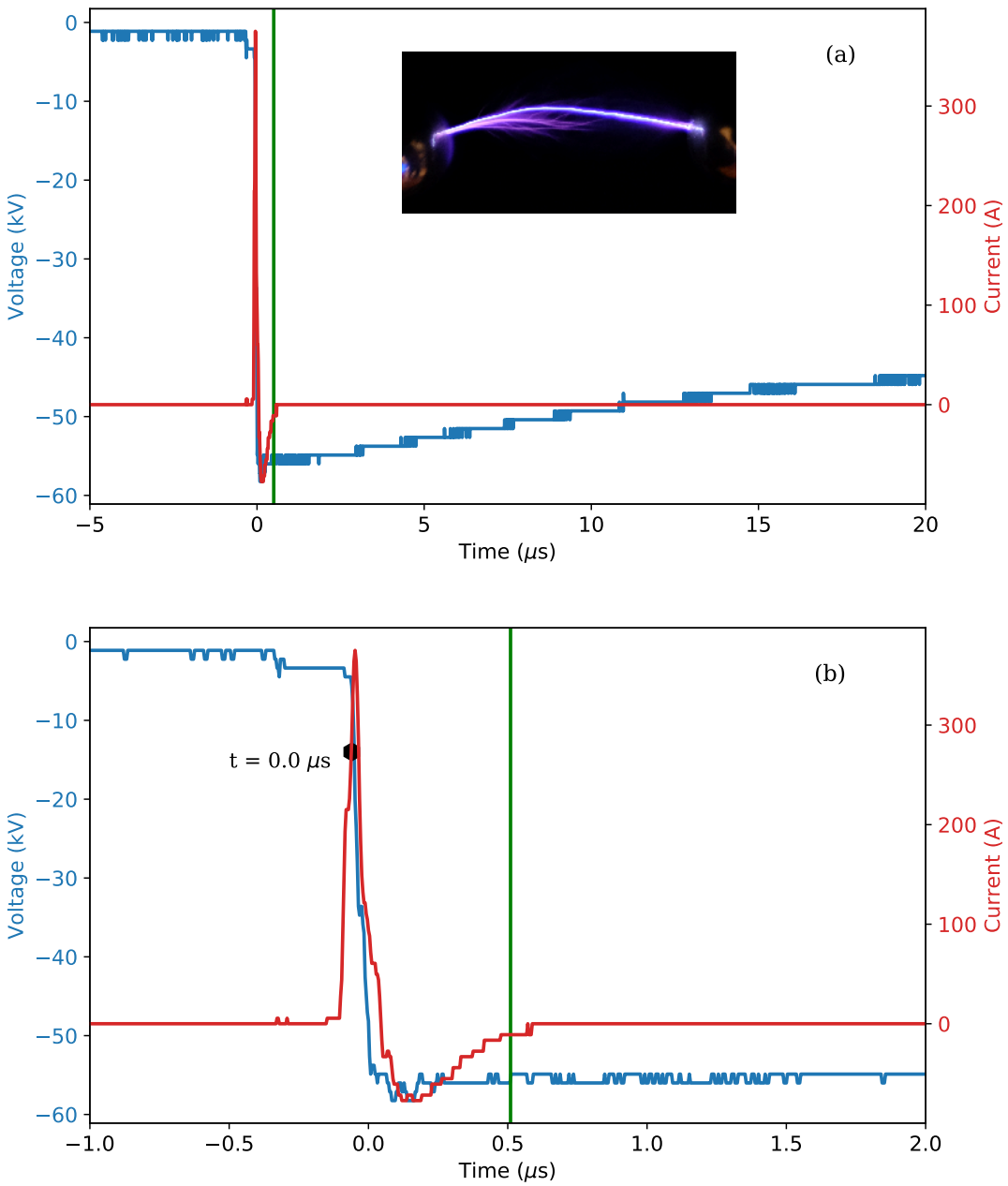

Figure S3. Measured voltage (blue line) and current (red line) during the generation of the small (4 cm long) spark discharge. (a) Complete time evolution of the voltage and current with an inset image showing the typical appearance of the small spark discharge. (b) Zoom in for a close view of the rise / decay region around 0.0 μs. The green line indicates the time of the first recorded spectrum. The black dot in (b) indicates the triggering time. The injected electric energy is 1.2 J or 30 J/m (since the discharge length is $\simeq$ 0.04 m).

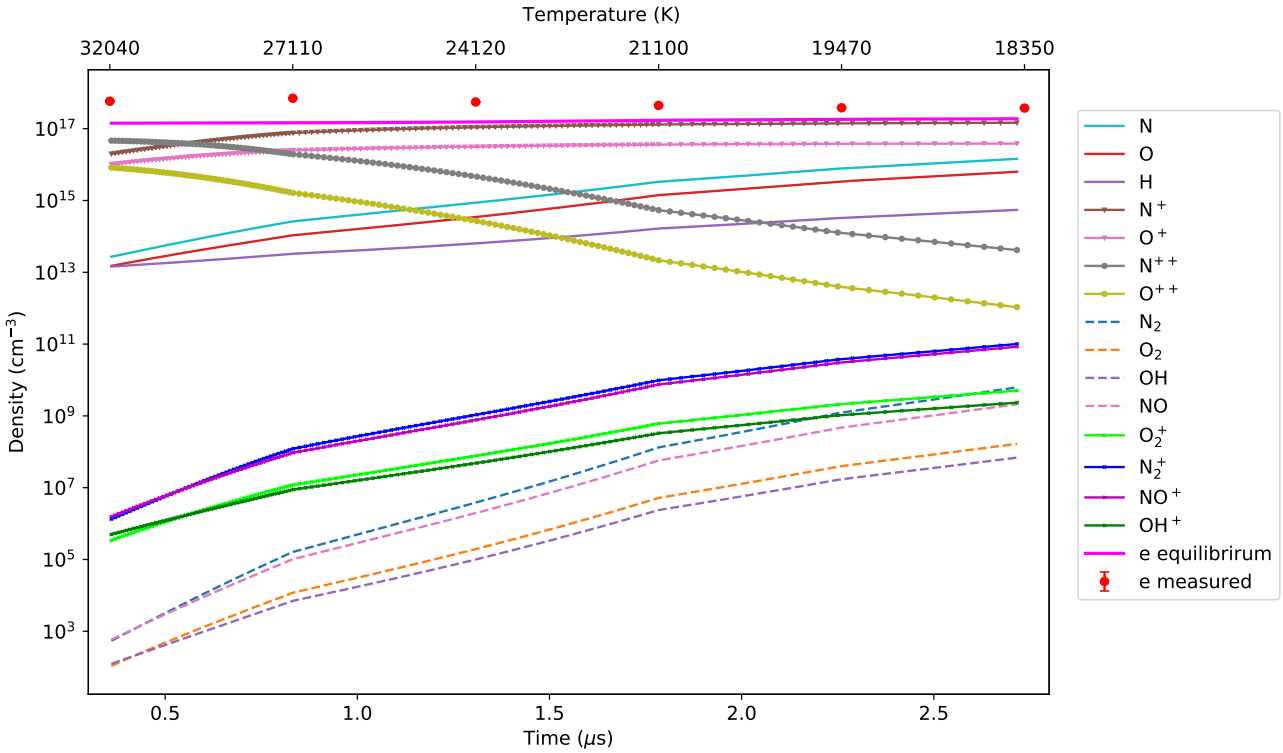

Figure S4. Measured electron density (red dots) in the SI lightning-like discharge and the equilibrium composition in a thermal plasma of humid (50 % RH) air at 1 atm (ambient pressure in Tarrasa, Spain). The figure shows the concentrations for a selection of neutral (atoms and molecules) and ionic (atomic and molecular) species as a function of time (bottom axis) and measured temperatures (top axis). The displayed times correspond to the different SI recorded spectra. The temperatures derived from each measured spectra are shown in the top axis. The measured electron densities can be recovered by multiplying the equilibrium electron densities at 1 atm by the δ_p factor for each time (see Figure 3 of main paper).

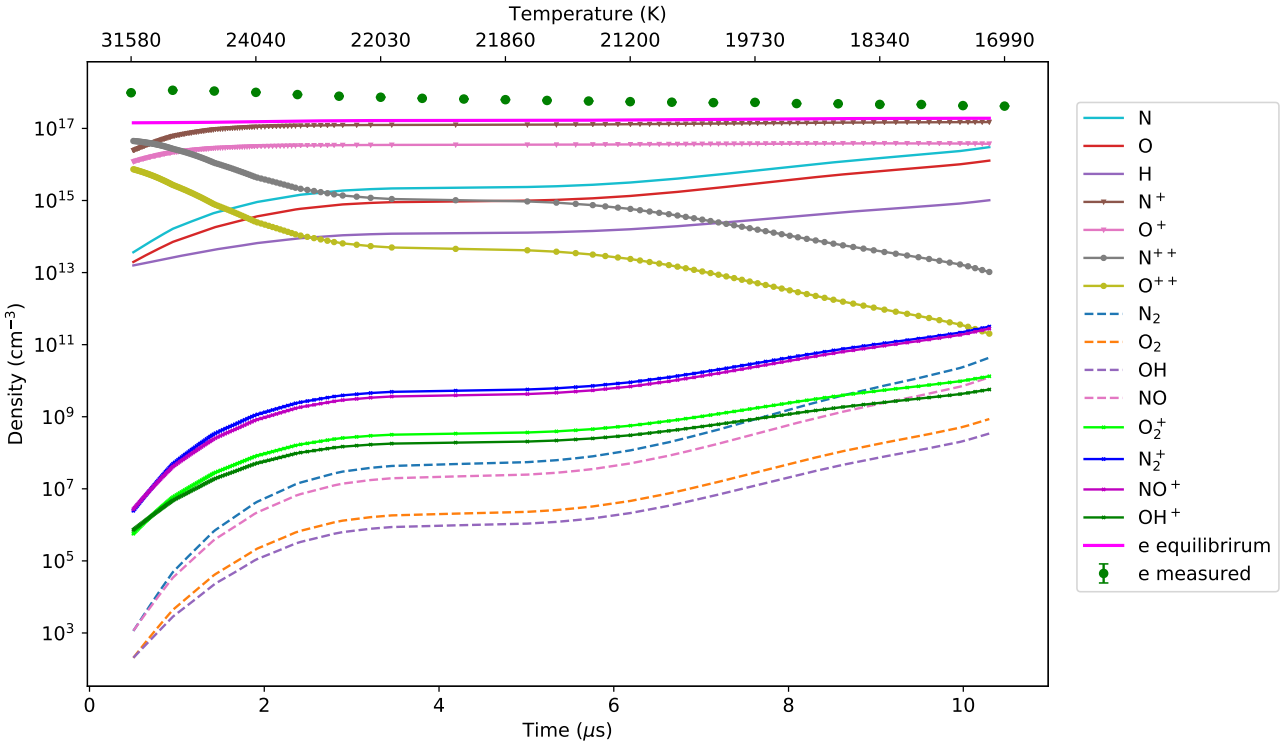

Figure S5. Measured electron density (green dots) in the LI lightning-like discharge and the equilibrium composition in a thermal plasma of humid (50 % RH) air at 1 atm (ambient pressure in Tarrasa, Spain). The figure shows the concentrations for a selection of neutral (atoms and molecules) and ionic (atomic and molecular) species as a function of time (bottom axis) and measured temperatures (top axis). The displayed times correspond to the different LI recorded spectra. The temperatures derived from each measured spectra are shown in the top axis. The measured electron densities can be recovered by multiplying the equilibrium electron densities at 1 atm by the δ_p factor for each time (see Figure 3 of main paper).

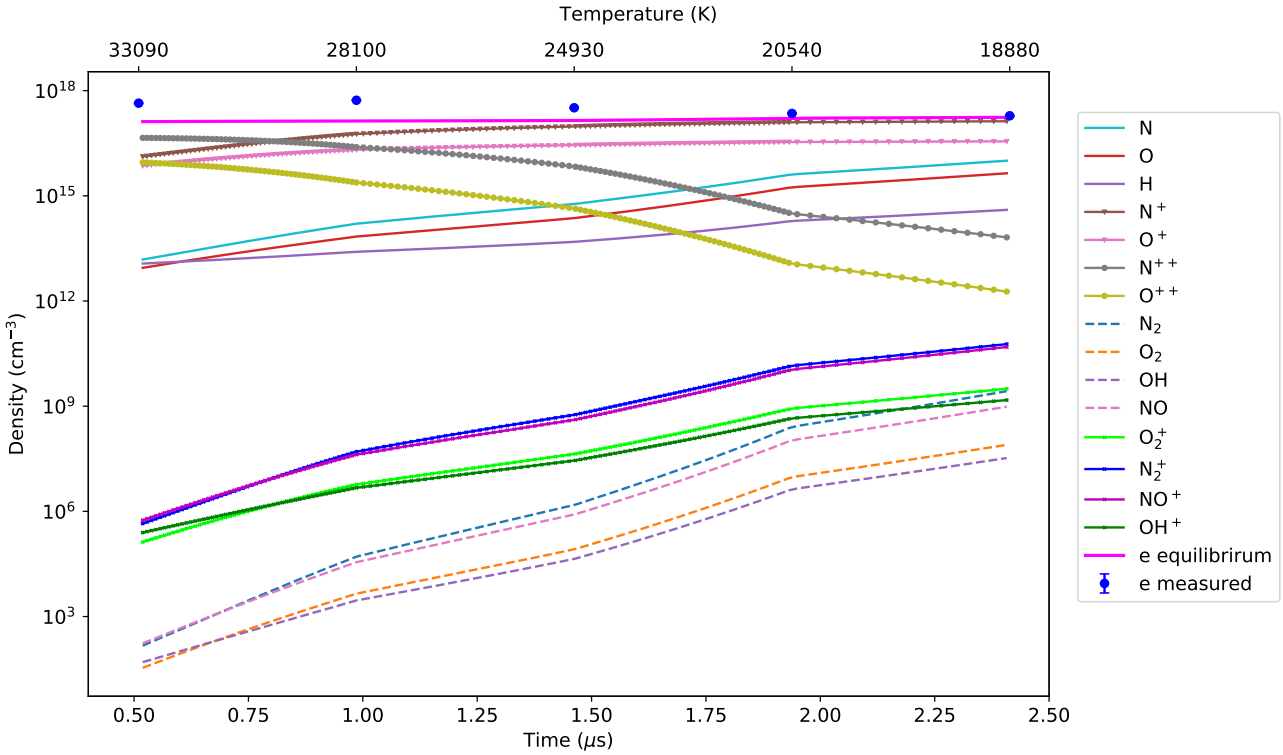

Figure S6. Measured electron density (blue dots) in the small spark discharge and the equilibrium composition in a thermal plasma of humid (50 % RH) air at 0.93 atm (ambient pressure in Granada, Spain). The figure shows the concentrations for a selection of neutral (atoms and molecules) and ionic (atomic and molecular) species as a function of time (bottom axis) and measured temperatures (top axis). The displayed times correspond to the different small spark measured spectra. The temperatures derived from each recorded spectra are shown in the top axis. The measured electron densities can be recovered by multiplying the equilibrium electron densities at 0.93 atm by the δ_p factor for each time (see Figure 3 of main paper).

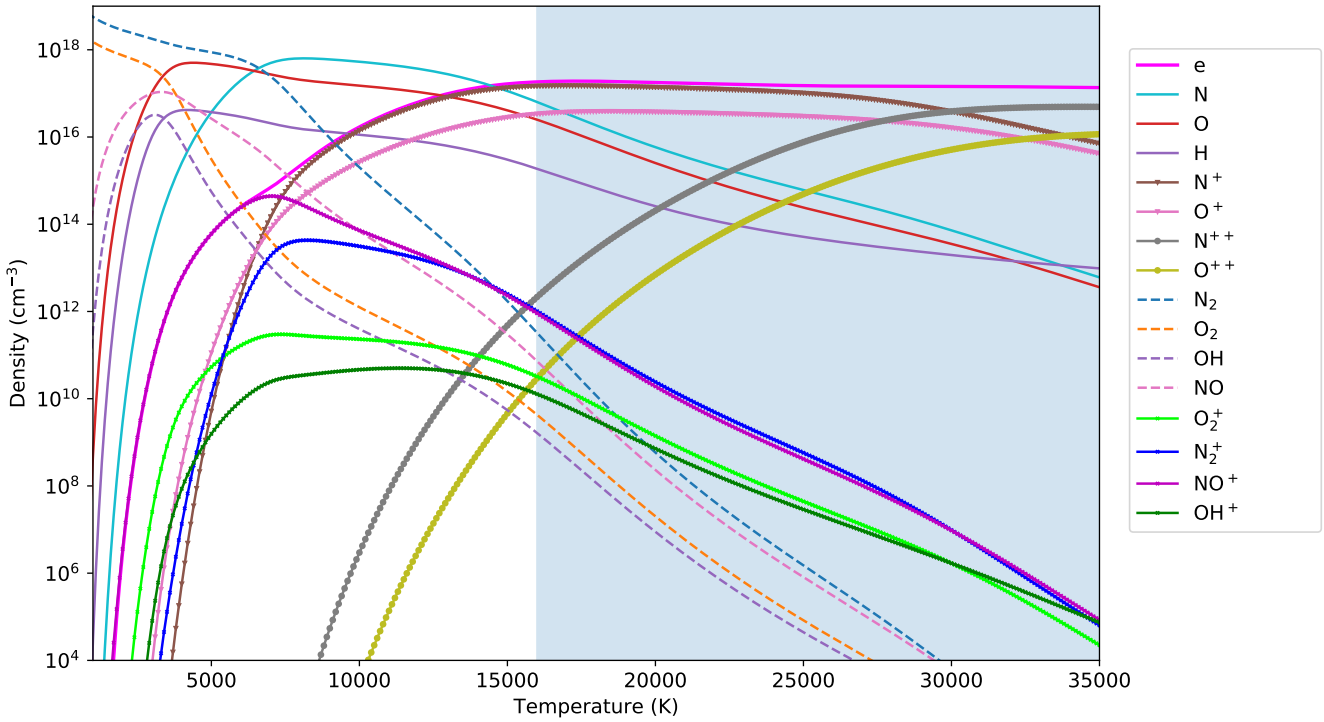

Figure S7. Equilibrium composition in an atmospheric pressure plasma of humid (50 % RH) air for gas temperatures between 1000 K and 35000 K. The figure displays the concentrations of the same species shown in Figures S4, S5 and S6. The bluish shadowed region indicates the variation of equilibrium densities within the approximate range of measured temperatures including temperatures above measured values due to possible underestimated temperature measurements.

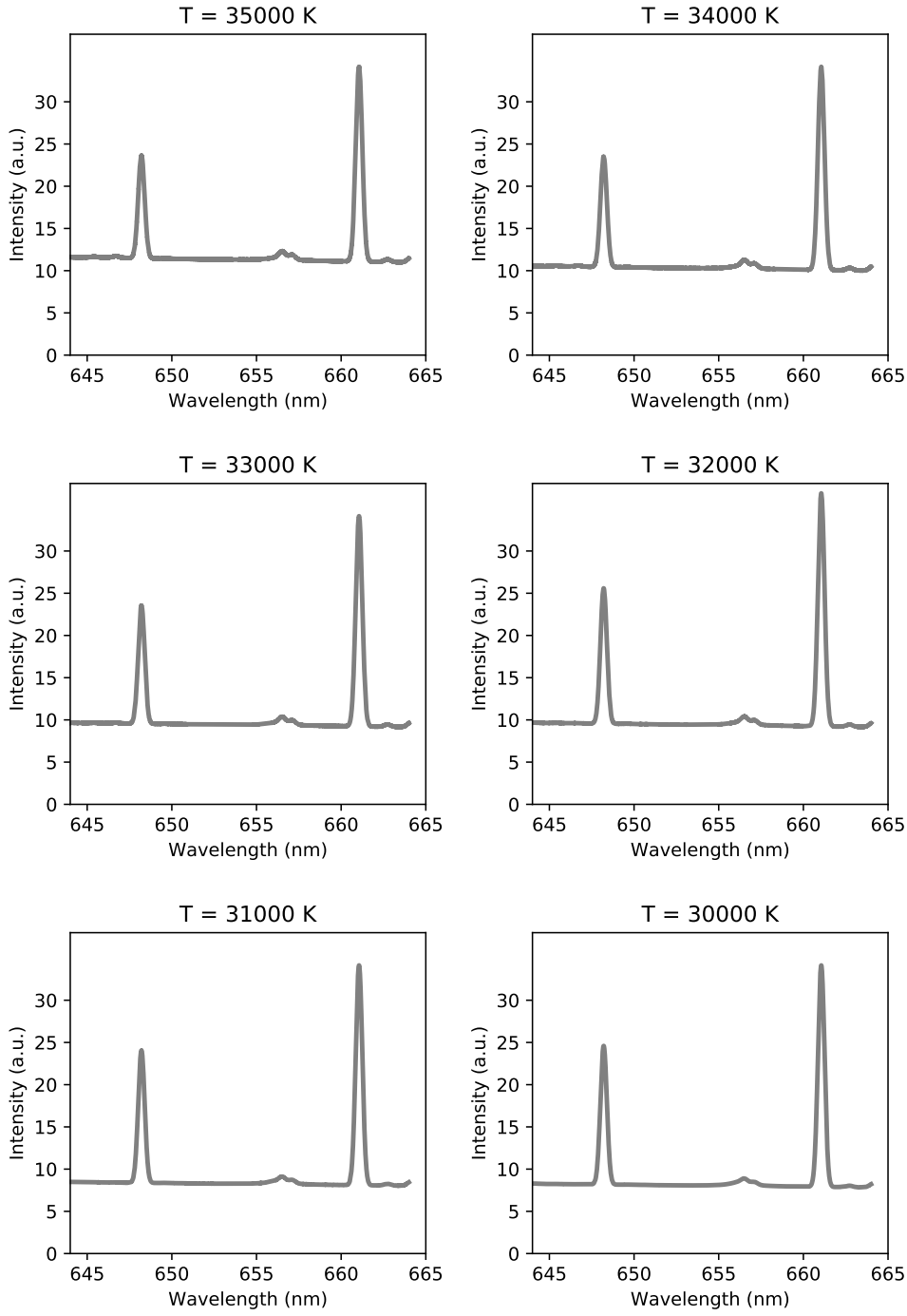

Figure S8. Synthetic spectra (645 nm - 665 nm) for an atmospheric pressure thermal plasma of humid (50 % RH) air for gas temperatures between 35000 K (top left) and 30000 K (bottom right). The figure illustrates the case of the meter long Switching Impulse (SI) discharge.

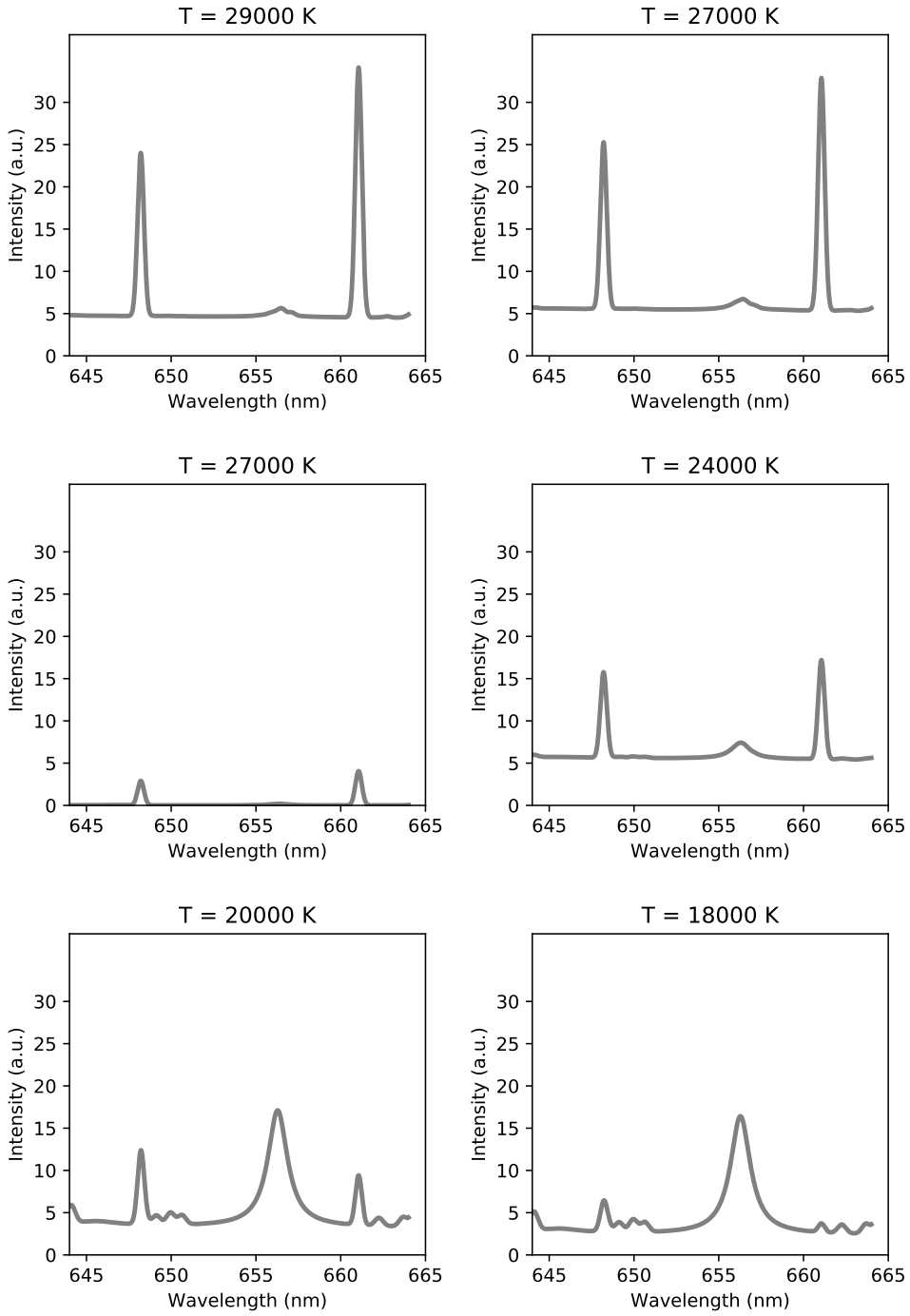

Figure S9. Synthetic spectra (645 nm - 665 nm) for an atmospheric pressure thermal plasma of humid (50 % RH) air for gas temperatures between 29000 K (top left) and 18000 K (bottom right). The figure illustrates the case of the meter long Switching Impulse (SI) discharge. Note that the case of 27000 K is shown with and without black body (continuum) radiation since no black body is seen in the measured spectra at -0.120 μs (see Fig S11).

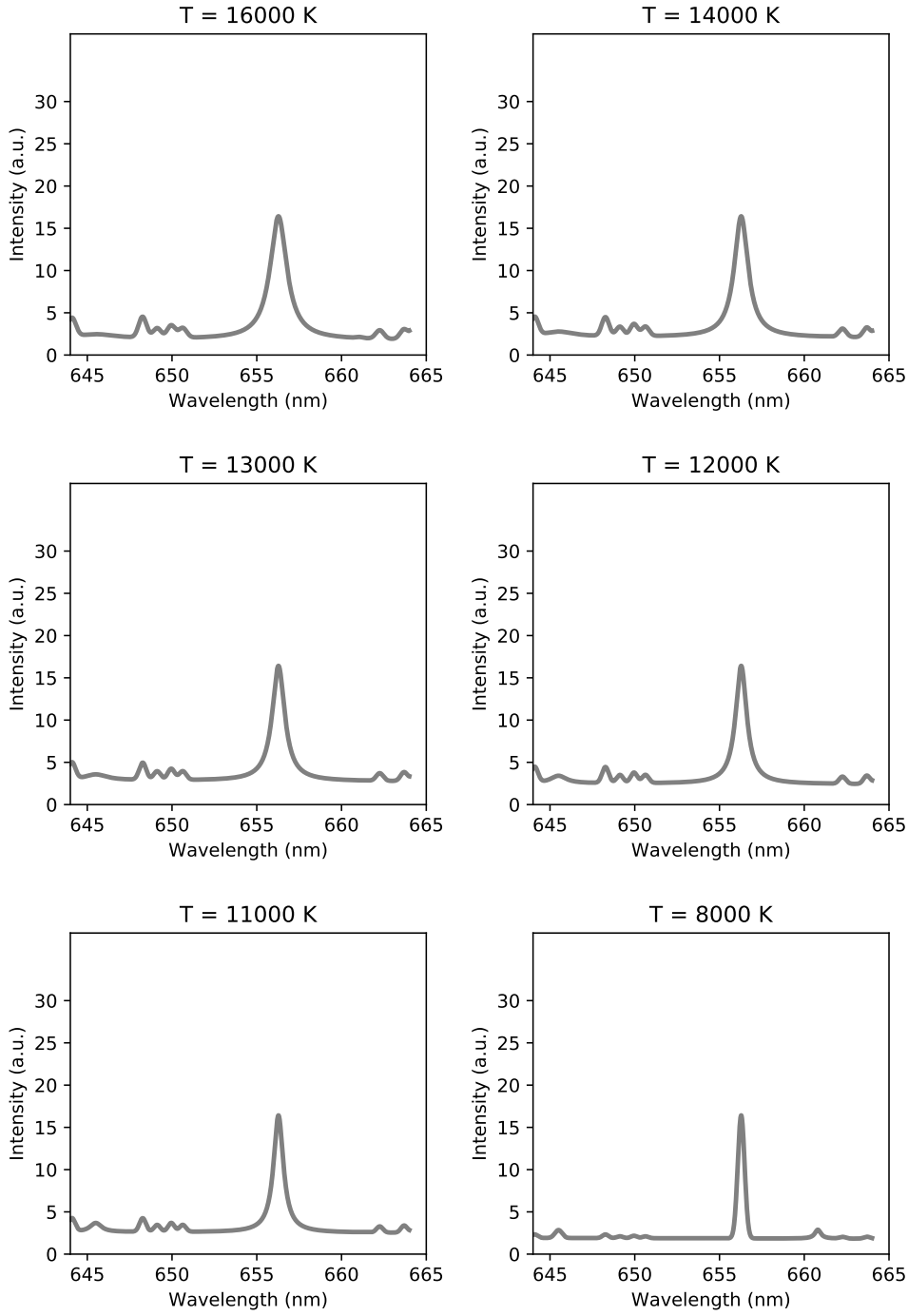

Figure S10. Synthetic spectra (645 nm - 665 nm) for an atmospheric pressure thermal plasma of humid (50 % RH) air for gas temperatures between 16000 K (top left) and 8000 K (bottom right). The figure illustrates the case of the meter long Switching Impulse (SI) discharge.

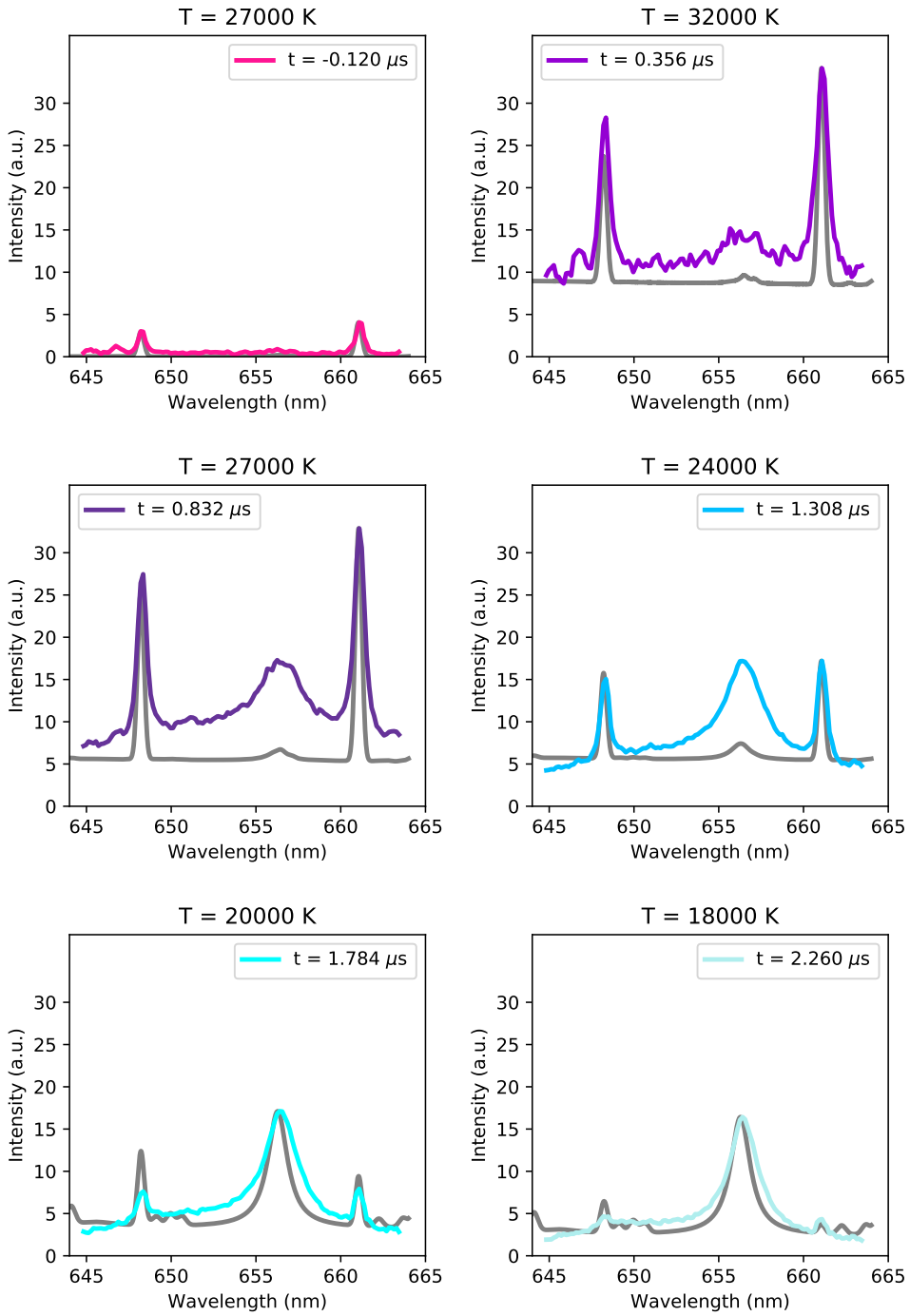

Figure S11. Comparison between calculated synthetic spectra (grey line) and measured spectra corresponding to the early times (from pre-trigger sub-μs to $\simeq$ 2.5 μs after triggering) of a meter long Switching Impulse (SI) discharge. Note that no black body emission is detected at -0.120 μs with 27000 K (see Figure 2(b) of the main paper for the time evolution of the measured temperatures).

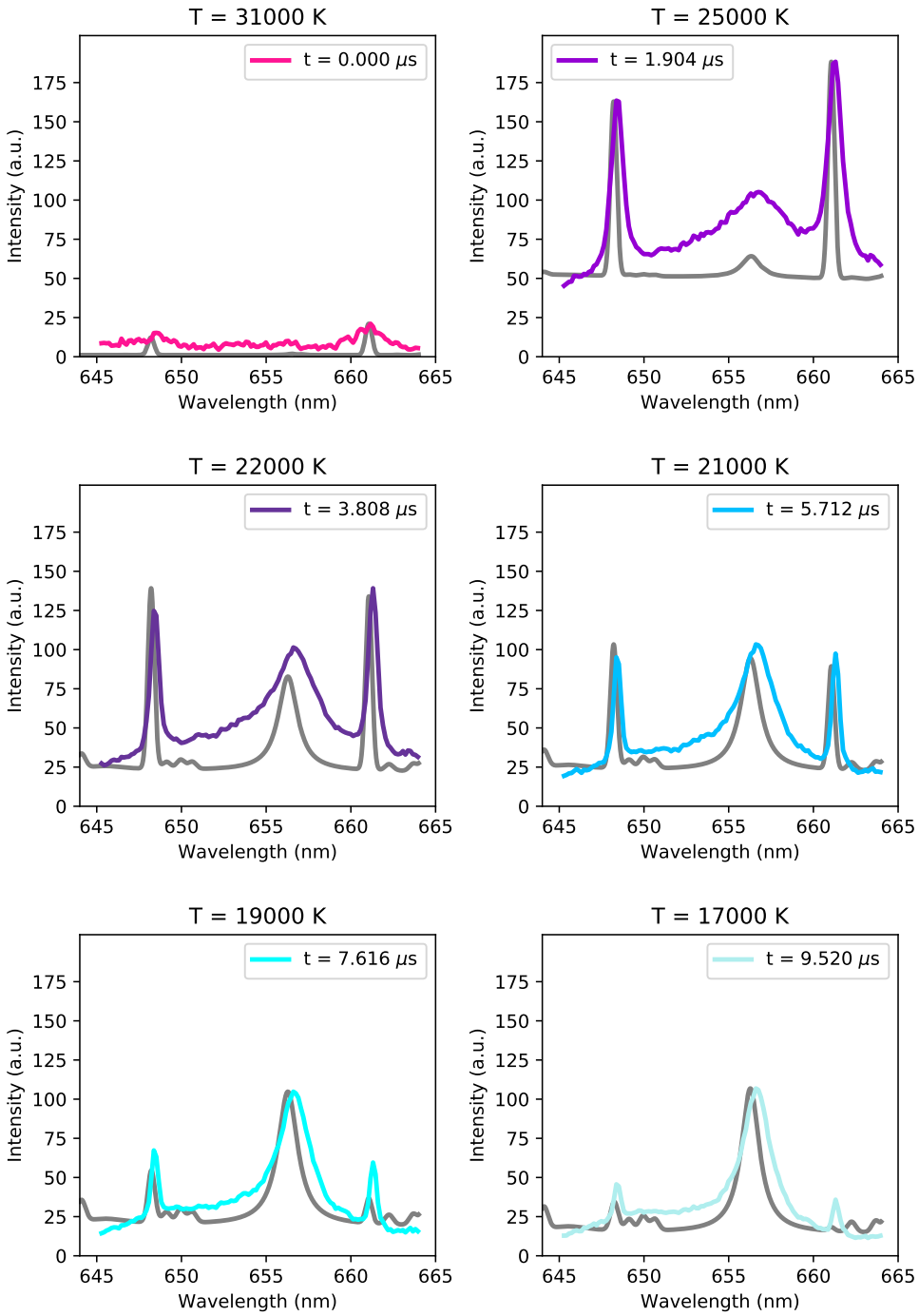

Figure S12. Comparison between calculated synthetic spectra (grey line) and measured spectra corresponding to the early times (from sub-μs to $\simeq$ 10 μs) of a meter long Lightning Impulse (LI) discharge. Weak black body emission is visible in the measured spectra at 0.0 μs with a measured temperature of 31000 K.

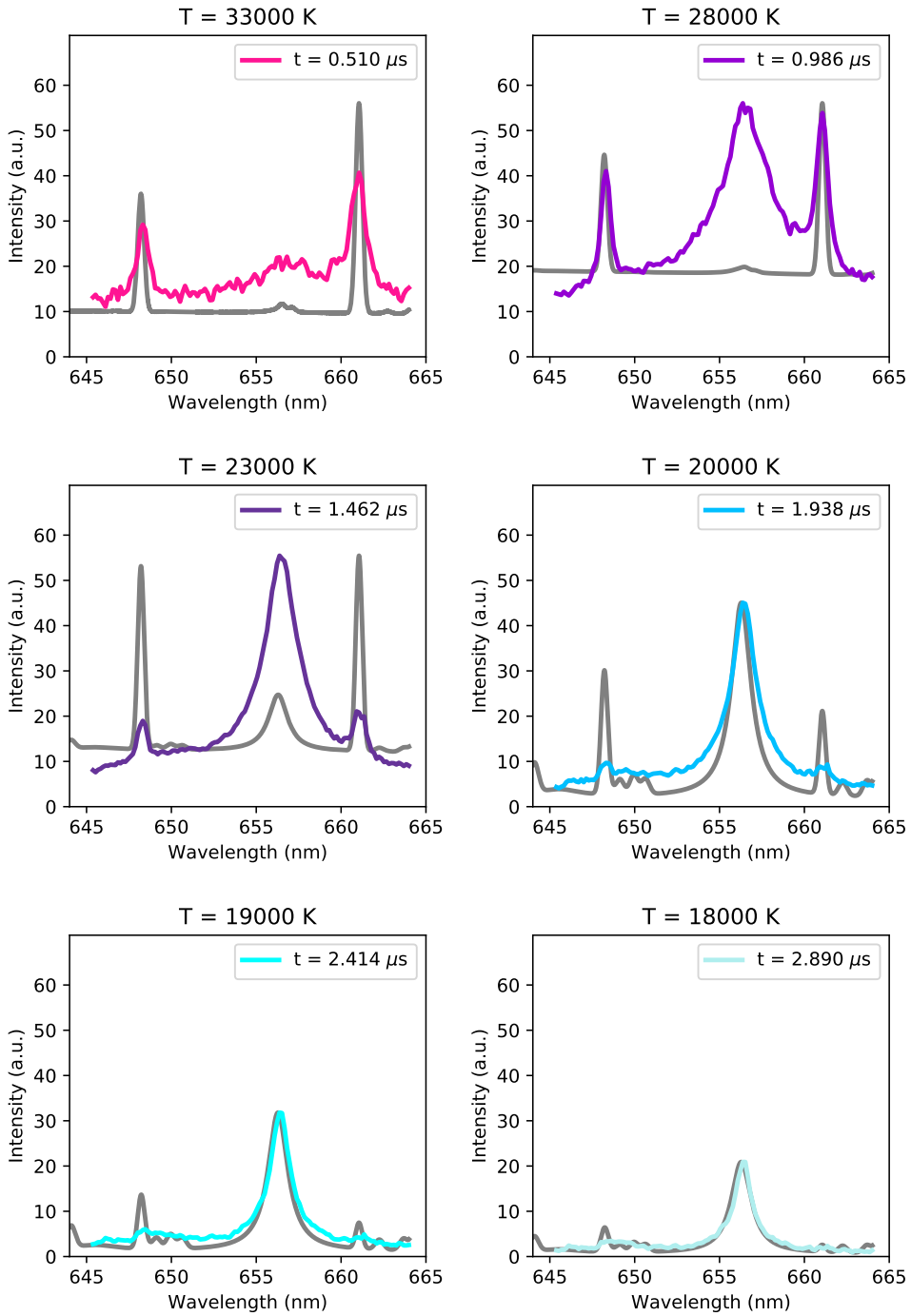

Figure S13. Comparison between calculated synthetic spectra (grey line) and measured spectra corresponding to the early times (from sub-μs to $\simeq$ 3 μs) of a small spark discharge.

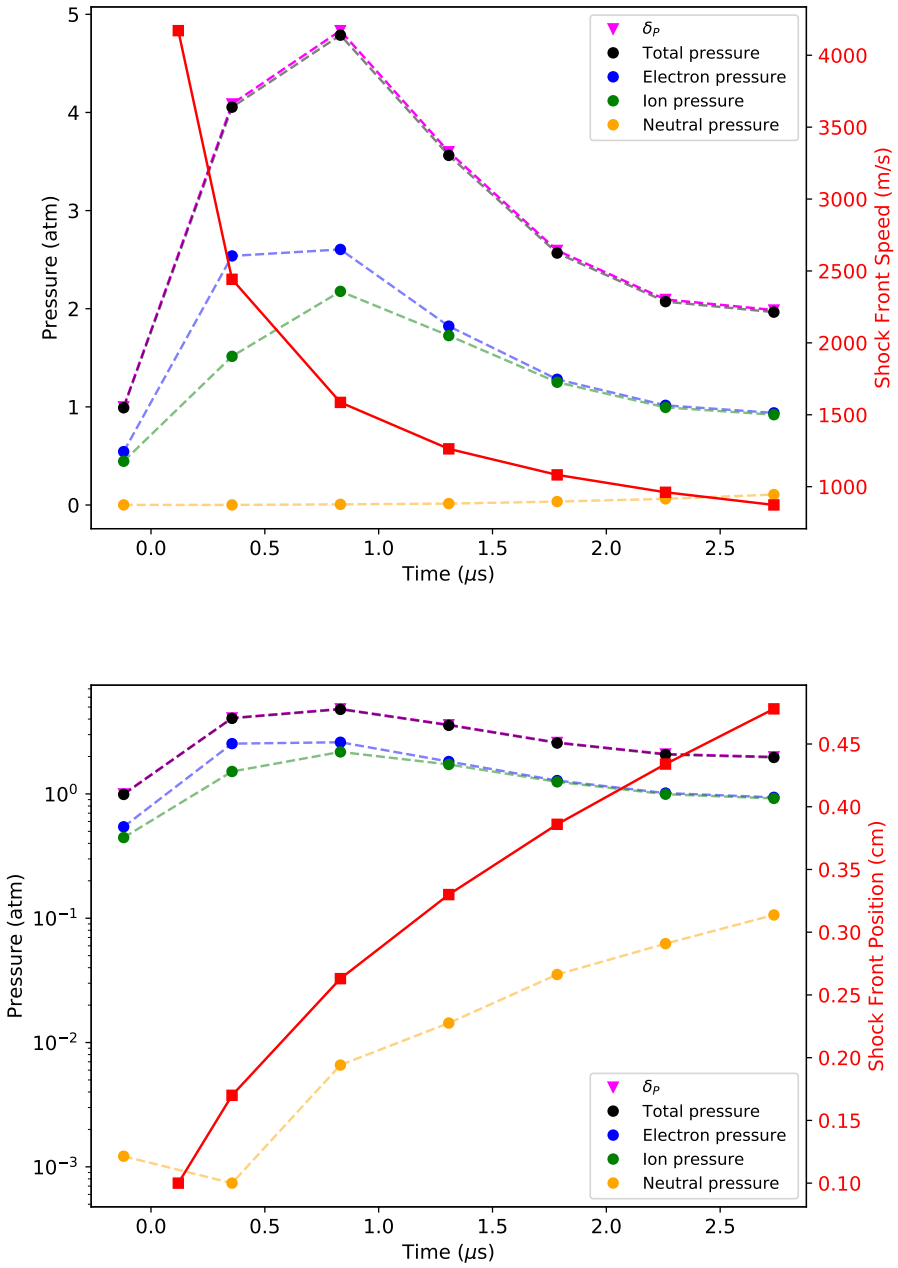

Figure S14. The factor δ_p, total pressure and partial pressures due to electrons, ions and neutrals as a function of time (left axis) in linear scale (top panel) and logaritmic scale (bottom panel). The right axis of the top and bottom panels include an estimation of the shock front speed (top panel) and shock front position (bottom panel) for the meter long SI discharge. Note that the pressure for -0.12 μs was represented assuming an equilibrium (at 1 atm) electron density as it is suggested from Figure S11 at -0.12 μs with 27000 K. Note also that the first value of the shock front position and speed are shown 240 ns after the pre-trigger time (-0.12 μs) for which the first image was recorded.

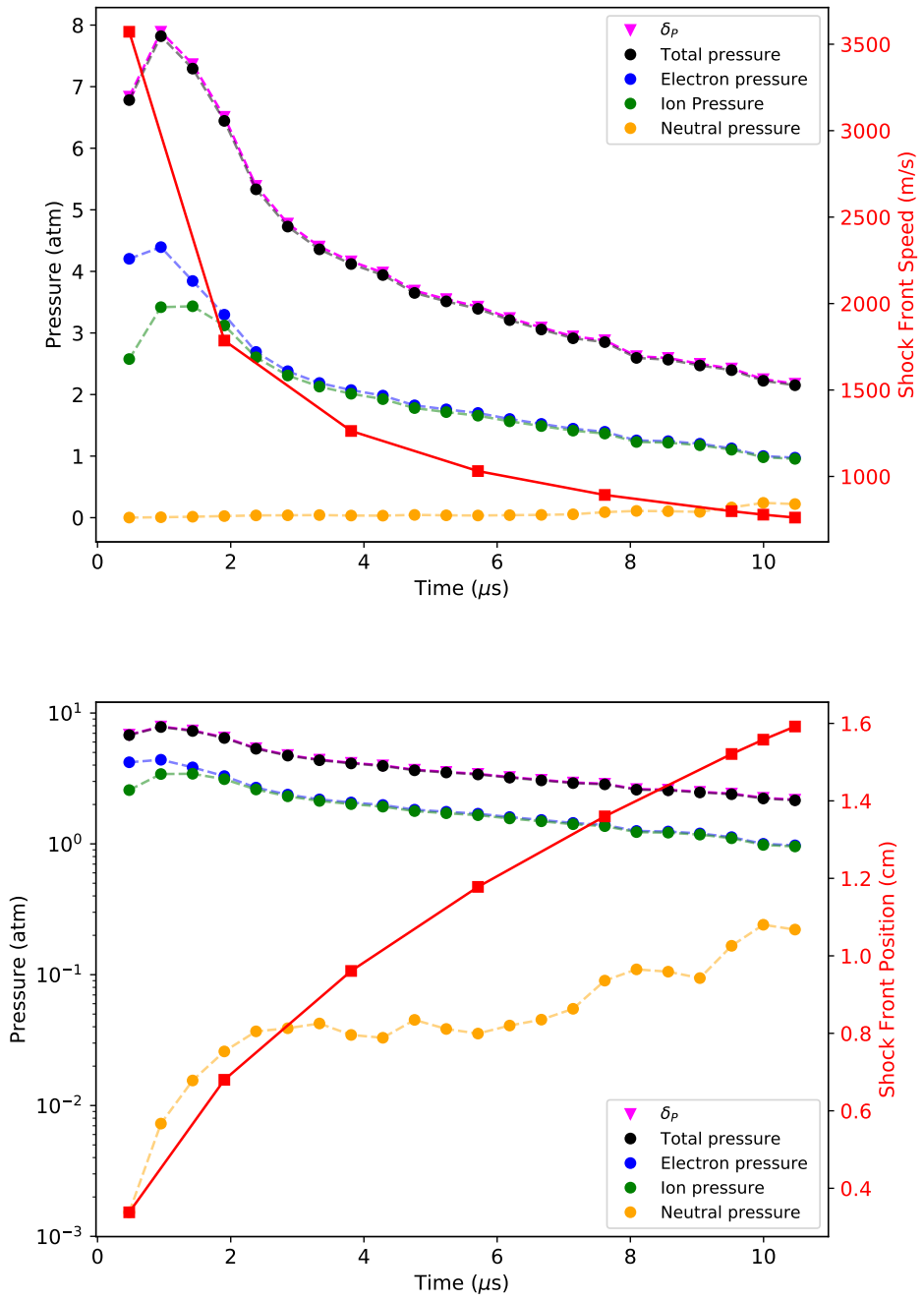

Figure S15. The factor δ_p, total pressure and partial pressures due to electrons, ions and neutrals as a function of time (left axis) in linear scale (top panel) and logaritmic scale (bottom panel). The right axis of the top and bottom panels include an estimation of the shock front speed (top panel) and shock front position (bottom panel) for the meter long LI discharge.

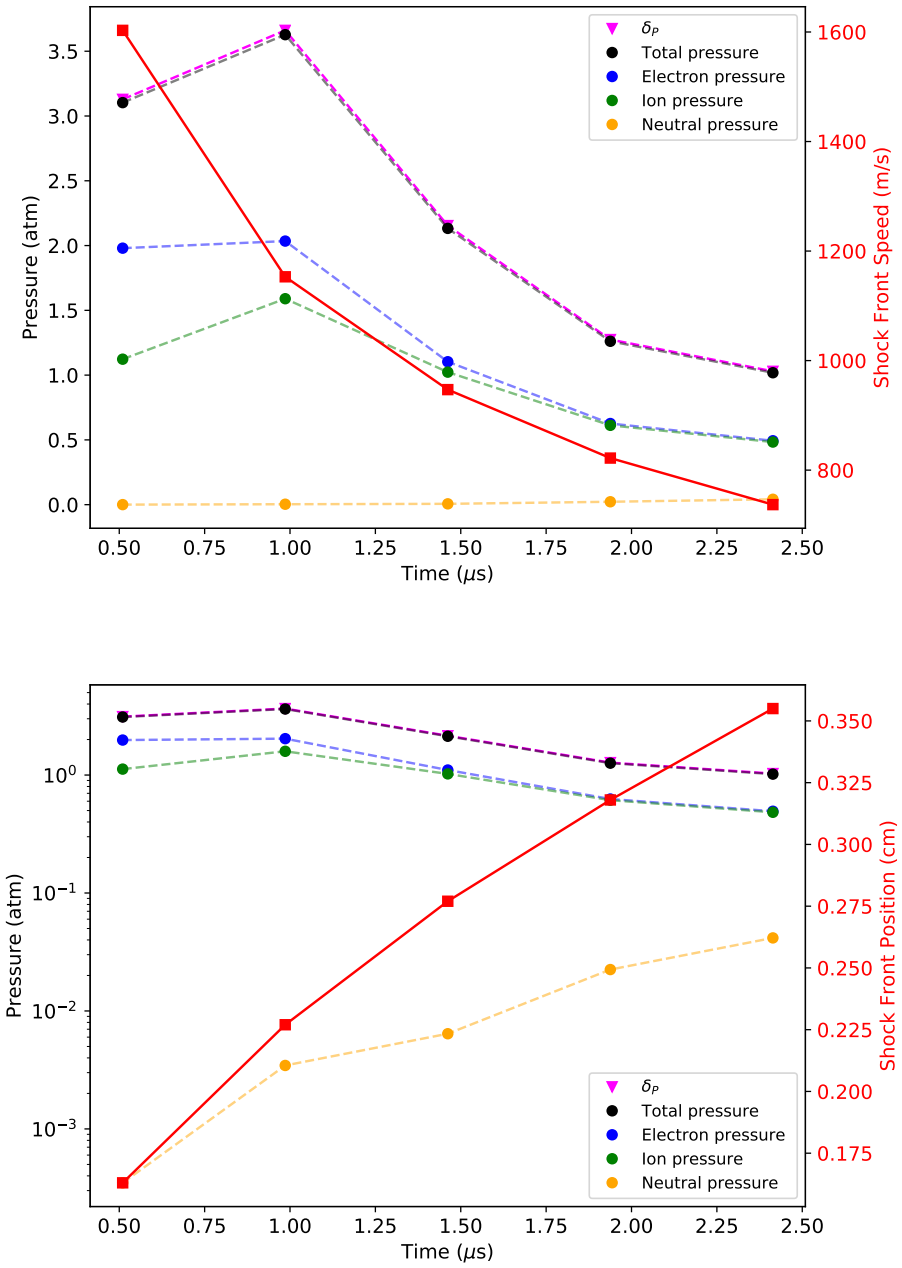

Figure S16. The factor δ_p, total pressure and partial pressures due to electrons, ions and neutrals as a function of time (left axis) in linear scale (top panel) and logaritmic scale (bottom panel). The right axis of the top and bottom panels include an estimation of the shock front speed (top panel) and shock front position (bottom panel) for a small (4 cm long) spark discharge.

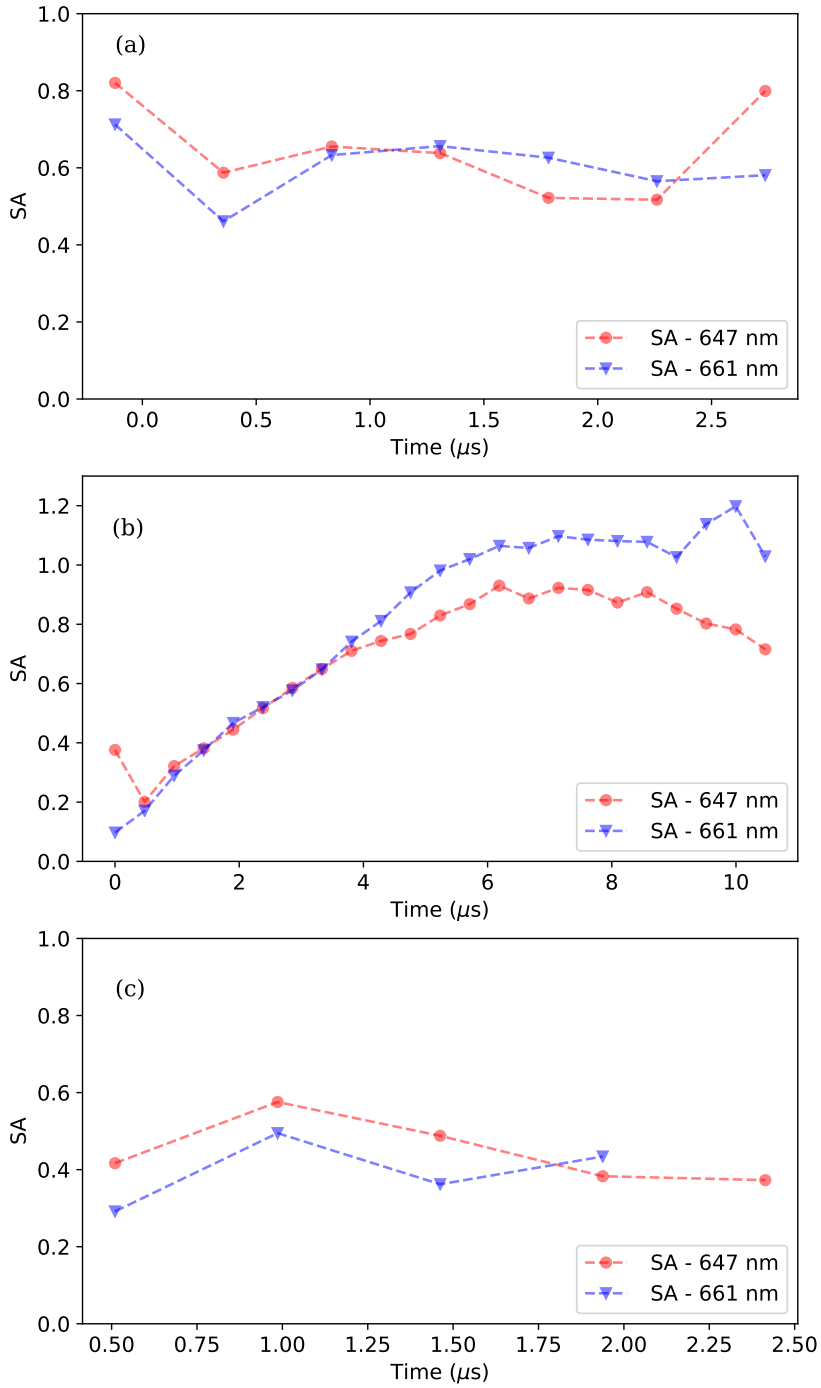

Figure S17. Self-absorption (SA) coefficient ($0 \leq \mathrm{SA} \leq 1$) of the 647 nm and 661 nm singly ionized N II lines as a function of time for meter long discharges SI (top panel) and LI (middle panel), and for a small (4 cm long) spark discharge (bottom panel). A SA = 1 indicates a complete optically thin line emission while SA = 0 applies for a complete optically thick line. The signal of the 661 nm ion line was not considered reliable after 2 μs.

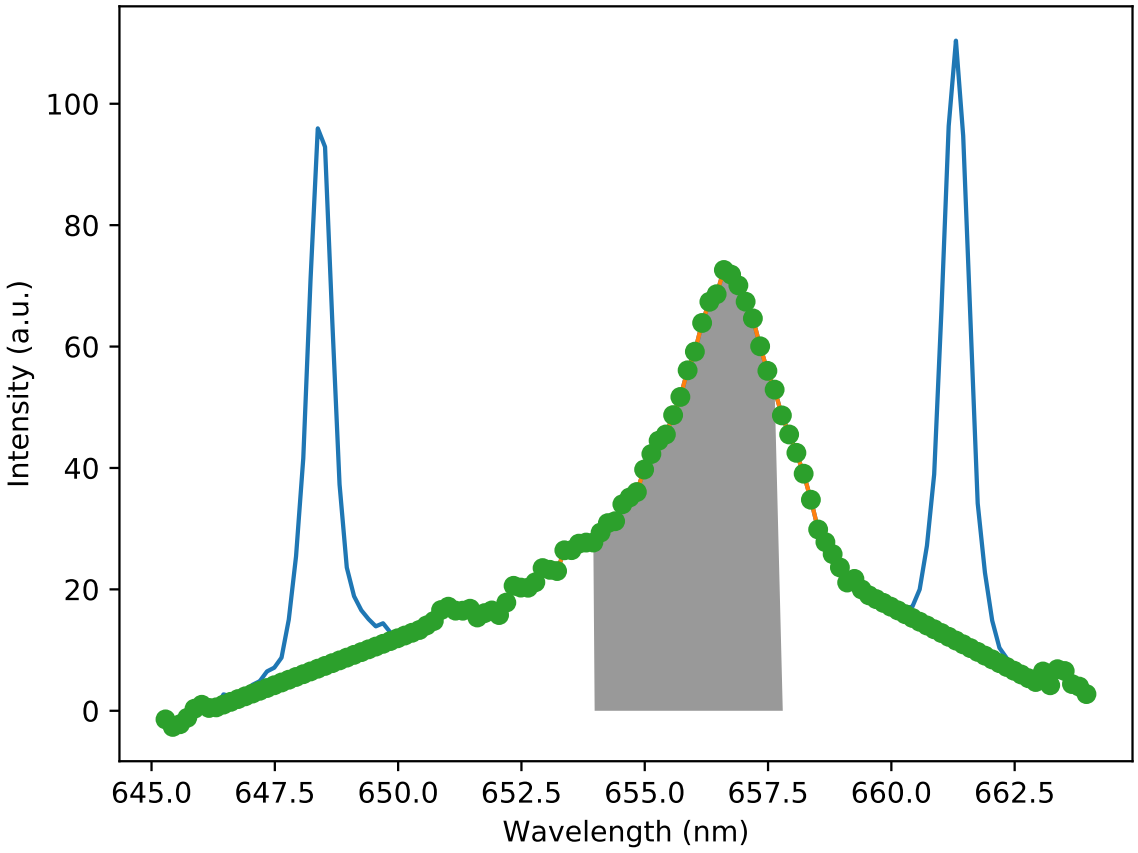

Figure S18. Illustration of the method followed to derive the electron density. The black body background is first subtrated. Due to the large electron density the broadening of the H_α line is large and it should be considered that it extends over the entire ($\simeq$ 20 nm) spectral range covered in our ultra high speed observations at 2.1 Mfps. Once the shape of the H_α (green dotted line) is determined, we compute the full width at half area (FWHA) (see grey shadow) under the green dotted line used to derived the measured electron density. The FWHA for the H_α is much less influenced by ion dynamics than the full width at half maximum (FWHM) and, consequently, it is a more reliable procedure (than using the FWHM) to obtain the electron density from the H_α line.

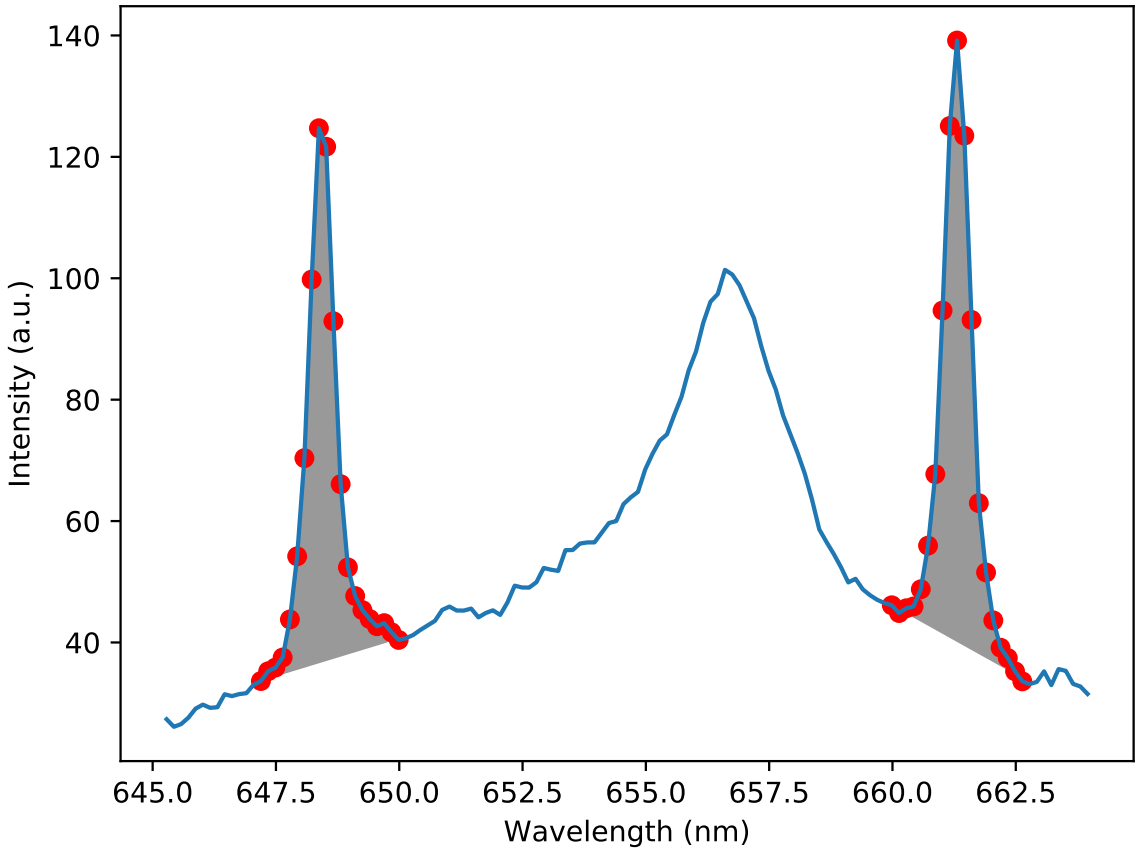

Figure S19. Illustration of the method followed to derive the electron temperature. To evaluate the electron temperature we only consider the intensity signal above the background (see red dots). We consider the total area (not the peak maximum) under the intensities of the 647 nm and 661 nm singly ionized N II lines.

Figure S20. Raw spectral image of the LI mode discharge generated with the Marx generator. This spectral image is 8 pixels height and 1024 pixels wide and was recorded at 2.1 Mfps. The difraction grating used has 1855 lines per mm and a spectral resolution of 0.38 nm.